Journal of Alloys and Compounds 1051 (2026) 185981

Contents lists available at ScienceDirect

Journal of Alloys and Compounds

journal homepage: www.elsevier.com/locate/jalcom

Yb/Er-doped Fe_3O_4@ZnO core@shell nanocomposites as multifunctional nanoplatforms for biomedical applications

Selin Bayram [a], Mehmet Fatih Akyel [a,b], Mustafa Burak Coban [c], Ayla Solmaz Avcikurt [d], Sinem Gultekin Tosun [d], Mehmet Emin Diken [e], Umit Huseyin Kaynar [f,g], Fatma Unal [a,h,*]

[a] Faculty of Engineering and Natural Sciences, Department of Biomedical Engineering, Samsun University, Samsun, Turkiye
[b] GEMPRO Medical Devices and Healthcare Products Co., Ltd., Samsun, Turkiye
[c] Faculty of Art and Sciences, Department of Physics, Balikesir University, Balikesir, Turkiye
[d] Faculty of Medicine, Department of Medical Biology, Balikesir University, Balikesir, Turkiye
[e] Faculty of Art and Sciences, Department of Molecular Biology and Genetic, Balikesir University, Balikesir, Turkiye
[f] Faculty of Engineering and Architecture, Department of Fundamental Sciences, Bakırcay University, Izmir, Turkiye
[g] Biomedical Technologies Design Application and Research Center, Bakırcay University, Izmir, Turkiye
[h] Vocational School of Technical Sciences, Samsun University, Samsun, Turkiye

ARTICLE INFO

Keywords:
Upconversion
Superparamagnetic behavior
Cytocompatibility
Biomedical applications
Core@shell nanocomposites
Lanthanide
Superparamagnetic

ABSTRACT

Fe_3O_4@ZnO and Yb/Er-doped Fe_3O_4@ZnO core@shell nanocomposites were rationally synthesized via a co-precipitation and modified Stöber route to achieve multifunctional performance for biomedical applications. Structural and morphological analyses confirmed crystalline Fe_3O_4 cores and ZnO shells, while lanthanide incorporation induced lattice expansion and enhanced agglomeration. Magnetic measurements revealed soft superparamagnetic-like behavior with suppressed coercivity and remanence, and the Fe_3O_4@4Yb5Er:ZnO composition exhibited increased magnetization due to the additive paramagnetic contribution of Yb^{3+}/Er^{3+} ions. Optical studies demonstrated efficient Yb^{3+}→Er^{3+} energy transfer under 980 nm excitation, generating bright green and red upconversion luminescence suitable for bioimaging. Antibacterial assays showed selective inhibition of *Staphylococcus aureus*, whereas *Escherichia coli* exhibited lower susceptibility. Cytocompatibility and gene expression analyses indicated that Fe_3O_4@4Yb5Er:ZnO promotes endothelial migration, angiogenic signaling, and extracellular matrix remodeling. Overall, these findings demonstrate that controlled lanthanide doping enables the integration of tunable magnetic, optical, antibacterial, and pro-angiogenic functionalities within a single nanosystem, underscoring their potential for theranostic and regenerative medicine applications.

1. Introduction

The development of multifunctional nanomaterials capable of integrating both diagnostic and therapeutic functionalities has become a central theme in contemporary biomedical research. Among these, superparamagnetic iron oxide nanoparticles (SPIONs), particularly magnetite (Fe_3O_4), have attracted extensive attention due to their high saturation magnetization, intrinsic biocompatibility, and excellent chemical stability. Fe_3O_4 nanoparticles further offer distinct advantages such as facile synthesis, tunable surface chemistry for functionalization, rapid magnetic responsiveness, low cytotoxicity, and cost-effective scalability, making them highly versatile candidates for a broad spectrum of biomedical applications [1–4]. They have been extensively applied as contrast agents in magnetic resonance imaging (MRI), mediators in magnetic hyperthermia, and carriers for the targeted delivery of therapeutic molecules such as drugs or nucleic acids [5–7]. However, bare Fe_3O_4 nanoparticles tend to oxidize and aggregate, leading to diminished performance and restricted biomedical applicability [8]. To overcome these limitations, core@shell architectures have been explored, where a protective and functional shell not only stabilizes the magnetic core but also imparts additional optical or biological functionalities.

Zinc oxide (ZnO), a wide-bandgap semiconductor (~3.37 eV), is considered an attractive shell material owing to its strong photoluminescence, photocatalytic activity, and broad-spectrum antibacterial properties. These features make ZnO highly versatile for applications

* Corresponding author at: Faculty of Engineering and Natural Sciences, Department of Biomedical Engineering, Samsun University, Samsun, Turkiye.
E-mail address: fatma.unal@samsun.edu.tr (F. Unal).

https://doi.org/10.1016/j.jallcom.2026.185981
Received 19 October 2025; Received in revised form 28 December 2025; Accepted 3 January 2026
Available online 4 January 2026

such as photocatalysis, biosensing, bacterial inhibition, and drug delivery [9–12]. Its biocompatibility and ability to generate reactive oxygen species (ROS) under UV/visible excitation make ZnO valuable for coatings, imaging, and antimicrobial applications [13]. The integration of ZnO as a shell around Fe_3O_4 nanoparticles therefore combines the superparamagnetism of the core with the luminescent and antibacterial features of the shell. Previous studies have demonstrated that Fe_3O_4@ZnO nanocomposites can serve as dual-functional systems for imaging and therapy, for example, enabling magnetic hyperthermia in cancer cells while simultaneously providing fluorescent signals for visualization [12,14]. These findings underscore the potential of Fe_3O_4-ZnO core@shell nanostructures as next-generation theranostic agents.

To further enhance the optical functionality of Fe_3O_4@ZnO nanocomposites, lanthanide doping has recently been introduced into ZnO shells. In particular, co-doping with Yb^{3+} and Er^{3+} ions enables upconversion luminescence (UCL), whereby low-energy near-infrared (NIR) photons are absorbed and subsequently converted into higher-energy visible emissions [15,16]. NIR excitation, especially at 980 nm, provides distinct advantages for bioimaging, including deeper tissue penetration, reduced light scattering, and significantly diminished background autofluorescence compared with conventional visible-light excitation, thereby greatly improving the sensitivity and reliability of *in vivo* imaging [17]. In our earlier work, Fe_3O_4@ZnO:RE nanocomposites were synthesized and their magneto-luminescent properties were confirmed under 532 nm excitation, highlighting their promise for bioimaging applications [15]. However, excitation in the visible region is limited by shallow penetration depth and background interference, restricting in vivo performance. The present study addresses this limitation by employing 980 nm excitation, which activates $Yb^{3+}\rightarrow Er^{3+}$ energy transfer processes, yielding strong green and red upconversion emissions. This transition from visible to NIR excitation significantly improves the biomedical relevance of these nanocomposites for deep-tissue imaging and theranostic applications.

Despite growing interest in Fe_3O_4@ZnO-based systems, most reported studies remain focused on their structural, magnetic, and optical properties, with limited exploration of their biological performance. In this work, we report the synthesis and comprehensive characterization of Fe_3O_4@ZnO and Yb/Er-doped Fe_3O_4@ZnO core@shell nanocomposites. Beyond structural and magneto-optical analyses, we systematically investigate their antibacterial activity against Gram-positive and Gram-negative bacteria, cytocompatibility using endothelial cells, effects on cell migration, and modulation of angiogenesis-related genes (VEGF, FGF, MMP-3, MMP-9). By integrating magnetic responsiveness, NIR-triggered upconversion luminescence, antibacterial effects, and pro-angiogenic cellular responses within a single nanoplatform, this study advances Fe_3O_4@ZnO:Yb/Er composites toward application as multifunctional nanoplatforms for bioimaging, regenerative medicine, and theranostics.

2. Materials and methods

The synthesis of multifunctional core@shell nanostructures was accomplished through a carefully designed two-step process, integrating co-precipitation and a modified Stöber method to achieve magnetic cores enveloped by a luminescent, bioactive shell. All chemical reagents were of analytical grade (≥98 % purity) and were used as received without any further purification. In the initial stage, superparamagnetic iron oxide nanoparticles (SPIONs) were generated by the co-precipitation of ferrous and ferric salts in aqueous medium. A stoichiometric mixture of iron (III) chloride hexahydrate ($FeCl_3{\cdot}6\ H_2O$) and iron (II) chloride tetrahydrate ($FeCl_2{\cdot}4\ H_2O$) was dissolved in 150 mL of deionized water, after which the pH was adjusted to approximately 9 by the gradual addition of 28 % NH_4OH solution. This adjustment triggered an immediate precipitation process, while ultrasonic agitation at 60°C for 15 min ensured homogeneous nucleation and particle growth. The characteristic black precipitates confirmed the formation of magnetite, which were subsequently collected using a neodymium magnet, washed repeatedly with deionized water to eliminate residual ions, and oven-dried at 80 °C.

In the second stage, the SPIONs cores were encapsulated within a lanthanide-doped ZnO shell using a modified Stöber route, thereby creating a well-defined core@shell architecture. For this purpose, the SPIONs were ultrasonically dispersed in a ternary solvent mixture of ethanol, deionized water, and NH_4OH, providing a colloidal environment favorable for controlled shell deposition. In parallel, zinc nitrate hexahydrate ($Zn(NO_3)_2{\cdot}6\ H_2O$), ytterbium nitrate pentahydrate ($Yb(NO_3)_3.5H_2O$), and erbium nitrate pentahydrate ($Er(NO_3)_3.5H_2O$) were dissolved in deionized water to form a transparent precursor solution. This precursor was added dropwise into the SPIONs suspension under continuous sonication, followed by 1 h of ultrasonic treatment to promote uniform coating and lanthanide incorporation within the ZnO lattice. The resulting nanocomposites were magnetically recovered, washed several times with ethanol and deionized water through centrifugation, and dried at 80 °C. Finally, a thermal treatment at 700 °C for 3 h was applied to induce crystallinity and enhance the structural stability of the core@shell system. A concise summary of the sample codes and chemical composition parameters is presented in Table 1, while the synthesis procedure is schematically illustrated in Fig. 1.

2.1. Materials characterization

The structural and functional properties of the synthesized Fe_3O_4@ZnO and Fe_3O_4@Yb,Er:ZnO composite nanoparticles were systematically investigated using a series of complementary techniques. The crystalline phase composition and degree of structural ordering were examined by X-ray diffraction (XRD) on a Philips PW3710 X'Pert Pro diffractometer, employing monochromatic CuK_α radiation (λ = 1.5406 Å) at an accelerating voltage of 40 kV and current of 30 mA. Diffraction patterns were collected in the 2θ range of 25°-60° at a scanning speed of 3° min^{-1}, enabling identification of the magnetite core reflections together with ZnO-related peaks. Chemical bonding environments and the presence of characteristic functional groups were investigated by Fourier-transform infrared spectroscopy (FT-IR, PerkinElmer Spectrum Two). The surface morphology and particle size distribution of the composites were analyzed using an FEI Quanta 650 Field Emission SEM operated at 20 kV accelerating voltage and a working distance of 9.8 mm, with images captured at magnifications of 20,000x, and 100,000x. To gain deeper insight into the internal structure and elucidate the formation of a well-defined core@shell architecture, Transmission Electron Microscopy (TEM) and High-Resolution TEM (HR-TEM) analyses were performed using an FEI TALOS F200S instrument operated at 200 kV. For TEM analysis, the synthesized nanocomposites were dispersed in ethanol and ultrasonicated for 10 min to obtain a homogeneous suspension. A drop of the suspension was then deposited onto carbon-coated copper grids and dried at room temperature prior to imaging. The magnetic response of the nanocomposites was investigated using a Vibrating Sample Magnetometer (VSM, Model 7407-Lakeshore). Room-temperature hysteresis loops were recorded under applied fields ranging from −10,000 to + 10,000 Oe, allowing comparative evaluation of the magnetic behavior between undoped and lanthanide-doped composites. Finally, the optical performance of the

Table 1
Sample codes, and chemical compositions of the core@shell nanocomposites.

Sample Designation	Chemical Composition (mol%)		
	Yb_2O_3	Er_2O_3	ZnO
Fe_3O_4@ZnO	0	0	100
Fe_3O_4@4Yb1Er:ZnO	4	1	95
Fe_3O_4@4Yb3Er:ZnO	4	3	93
Fe_3O_4@4Yb5Er:ZnO	4	5	91

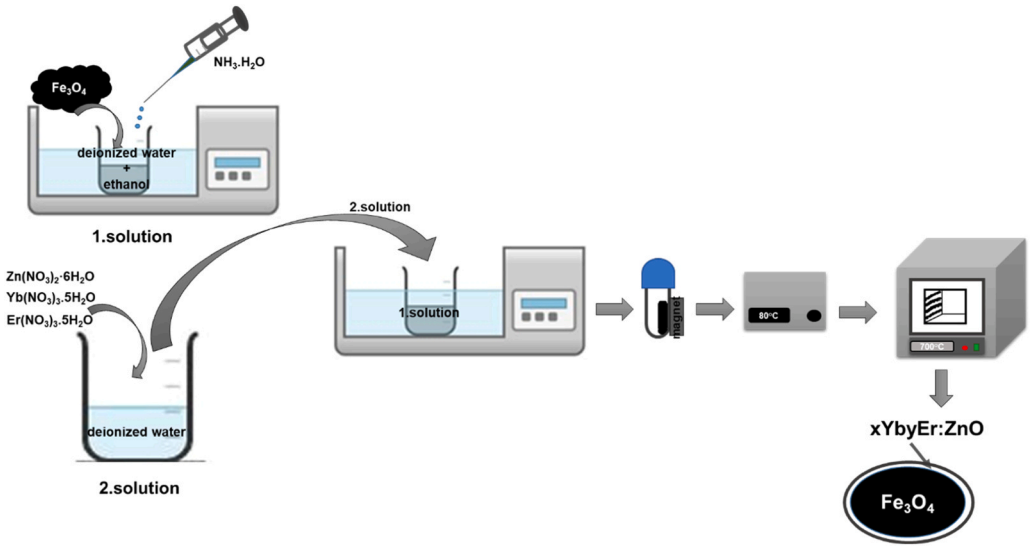

Fig. 1. Schematic illustration of the synthesis of core@shell nanocomposites.

materials was assessed through upconversion photoluminescence (UCL) spectroscopy. UCL measurements were performed using a FS5 spectrofluorometer under 980 nm excitation, and the corresponding emission spectra confirmed the distinct upconversion behavior imparted by the lanthanide co-doped ZnO shells.

2.2. Cell culture

Human umbilical vein endothelial cells (HUVEC; ATCC PCS-100–010) were cultured in Dulbecco's Modified Eagle Medium (DMEM; Cat. No: 41966–029; Gibco, Thermo Fisher Scientific, USA) supplemented with L-glutamine and 10 % fetal bovine serum (FBS; Cat. No: A5256701; Gibco, Thermo Fisher Scientific, USA). All cultures were maintained at 37 °C in a humidified atmosphere containing 5 % CO_2.

2.3. MTT assay

Fe_3O_4@4Yb1Er:ZnO, Fe_3O_4@4Yb3Er:ZnO, and Fe_3O_4@4Yb5Er:ZnO nanocomposites were suspended in DMEM at 100 mg/mL and homogenized to obtain uniform particles, followed by dilution to 10 mg/mL stock solutions. Control cells received no treatment, while experimental groups were exposed to 50, 100, 200, 400, and 800 μg/mL of each nanoparticle. To eliminate potential microorganisms, nanoparticle samples were sterilized under 254 nm UV-C light for 1 h on both sides. Prior to application, nanoparticles were gently mixed by pipetting to ensure homogeneity and minimize absorbance interference, then transferred to 96-well plates. All treatments were performed in triplicate, and cells were incubated at 37 °C with 5 % CO_2 for 24, 48, and 72 h.

Cytotoxicity was evaluated using the MTT assay. At the end of each incubation period, cells were incubated with 0.5 mg/mL MTT at 37 °C for 4 h. The resulting blue formazan crystals were dissolved in isopropanol containing 0.008 M HCl, and absorbance was measured at 570 nm using a Thermo Multiskan Go spectrophotometer.

2.4. Cell migration analysis (Scratch assay)

HUVECs from control and nanocomposites-treated groups were seeded in 6-well plates at 1×10^6 cells per well and cultured overnight at 37 °C in 5 % CO_2. When monolayers reached approximately 80 % confluence, a straight scratch was made using a sterile 200 μL pipette tip. Control cells received no treatment, while treated cells were exposed to nanoparticle doses determined from the MTT assay. Following scratching, cells were washed with 2 mL PBS to remove debris and smooth the edges, then incubated in DMEM supplemented with 10 % FBS. Images were captured immediately (0 h) and 24 h post-scratch to monitor proliferation and migration. Experiments were performed in triplicate.

2.5. RNA isolation and quantitative gene expression analysis

To assess the effects of Fe_3O_4@4Yb1Er:ZnO, Fe_3O_4@4Yb3Er:ZnO, and Fe_3O_4@4Yb5Er:ZnO nanocomposites on the mRNA levels of MMP-3, MMP-9, VEGF, and FGF relative to control, total RNA was isolated from cells collected at 24, 48, and 72 h using the GeneJET RNA Purification Kit (Cat. No: K0731; Thermo Scientific, USA). RNA purity and concentration were measured using a NanoDrop spectrophotometer, and samples with A260/A280 ratios of 1.8–2.0 were used for downstream analysis. Complementary DNA (cDNA) was synthesized from 1 μg of total RNA using the OneScript® Plus cDNA Synthesis Kit (Cat. No: G236; Applied Biological Materials Inc., Canada) following a three-step protocol: primer annealing at 25 °C for 10 min, reverse transcription at 50 °C for 15 min, and reaction termination at 85 °C for 5 min.

qRT-PCR was performed using BlasTaq 2X qPCR MasterMix (Cat. No: G891; Applied Biological Materials Inc., Canada) in a total volume of 20 μL on a CFX96 Touch Real-Time PCR Detection System (Bio-Rad, USA). The cycling program included an initial denaturation at 95 °C for 3 min, followed by 40 cycles of 95 °C for 15 s and 60 °C for 1 min. All reactions were conducted in technical triplicates with negative controls. Relative gene expression levels were normalized to β-actin and calculated using the $2^{-\Delta\Delta CT}$ method. Primer sequences used for gene expression analysis were given in Table 2.

2.6. Statistical analysis

All data were obtained from at least three independent experiments, and results are presented as mean ± standard deviation (SD). Statistical analyses were performed using SPSS version 20 (IBM Corp., Armonk, NY, USA). One-way analysis of variance (ANOVA) was applied for multiple group comparisons, and pairwise comparisons for parameters showing significant differences were conducted using Tukey's HSD post-hoc test. A p-value of less than 0.05 was considered statistically significant.

2.7. Antibacterial activity

The antibacterial performance of the synthesized Fe_3O_4@ZnO and

Table 2
Primer sequences used for gene expression analysis.

Primer Name	Forward	Reverse
MMP-3	5′-CACTCACAGACCTGACTCGGTT-3′	5′-AAGCAGGATCACAGTTGGCTGG-3′
MMP-9	5′-TTCCAAACCTTTGAGGGCGA-3′	5′-CAAAGGCGTCGTCAATCACC-3′
VEGF	5′-AGGAGGAGGGCAGAATCATCA-3′	5′-CTCGATTGGATGGCAGTAGCT-3′
FGF	5′-GGAGAAGAGCGACCCTCACATCA-3′	5′-GCCAGGTAACGGTTAGCACACACT-3′
β-actin	5′-CCAACCGCGAGAAGATGA-3′	5′-CCAGAGGCGTACAGGGATA-3′

Fe_3O_4@Yb,Er:ZnO nanocomposites was systematically assessed against *Staphylococcus aureus* (Gram-positive) and *Escherichia coli* (Gram-negative) using the agar well diffusion method. Fresh bacterial cultures were grown in Mueller Hinton Broth and adjusted to a final concentration of approximately 1×10^5 CFU/mL. Subsequently, wells of 6 mm diameter were carefully prepared on Mueller Hinton Agar plates, into which 10 mg of each nanocomposite sample was introduced. The inoculated plates were then incubated at 37 °C for 18–24 h under aerobic conditions. After incubation, the antibacterial efficacy was determined by measuring the diameters of the inhibition zones surrounding each well. Zone sizes were quantified using the ImageJ software to ensure precision in evaluation. All experiments were performed in triplicate, and the presence of a distinct inhibition halo around the wells was considered indicative of effective antibacterial activity of the tested nanocomposites.

3. Results and discussions

3.1. Structural analysis

Fig. 2 presents the XRD patterns of undoped and ZnO nanocomposites doped with 4 mol% Yb and 5 mol% Er. In the diffractograms, the peaks corresponding to the Fe_3O_4 and ZnO phases are marked with "*" and "+", respectively. All composite nanoparticles exhibited distinct diffraction peaks belonging to the cubic Fe_3O_4 core (JCPDS card no: 075–0449, space group *Fd-3m*) and the hexagonal ZnO shell (JCPDS card no: 079–0208, space group *P6₃mc*), confirming the crystalline nature of both components. The Fe_3O_4 phase exhibited characteristic diffraction peaks at 2θ values of 29.36°, 35.25°, 42.89°, 48.95°, 53.67°, and 58.42°, corresponding to the (220), (311), (400), (331), (422), and (511) planes, respectively. The ZnO phase showed its main reflections at 2θ values of 31.81°, 34.36°, 36.25°, 47.53°, and 56.78°, which are attributed to the (100), (002), (101), (102), and (110) planes, respectively. Notably, no additional diffraction peaks or impurity-related signals were detected, indicating the absence of secondary phases, and confirming the phase purity of the synthesized composite nanoparticles.

The inset shows a magnified view of the (101) diffraction peak of the ZnO phase located near 2θ ≈ 36.25°, where a clear shift toward the lower-angle side is observed upon Yb^{3+} and Er^{3+} doping. This shift is clearly marked with an arrow in the inset of the graph, highlighting the leftward movement in the doped sample (Fe_3O_4@4Yb5Er:ZnO) compared to the undoped sample. Such a shift is indicative of lattice expansion, which is attributed to the substitution of Zn^{2+} ions (ionic radius: 0.74 Å) with larger lanthanide ions, Yb^{3+} (0.858 Å) and Er^{3+} (0.881 Å) [18–20]. The incorporation of these ions into the ZnO crystal lattice causes local structural distortion and an increase in lattice parameters, further confirming the successful doping of the ZnO shell with Yb and Er ions.

The functional groups obtained by FTIR spectra were analyzed on dried magnetite samples using an FTIR – Shimadzu 8400 spectrophotometer with a range of wavenumbers 4000–400 cm^{-1}, as shown in Fig. 2(b). A series of well-defined absorption bands corresponding to the intrinsic vibrational modes of the Fe-O, C-O/C-H, and O-H units, which constitute the characteristic building blocks of the Fe_3O_4:ZnO core-shell structure, were observed in the range of 461–1475 cm^{-1}. All nanoparticles exhibit the vibration of the octahedral Fe-O bond at approximately 461 cm^{-1}, which is attributed to the formation of Fe_3O_4 through Fe-O bonding [21]. The characteristic feature of the O-H bond outside the bond plane, observed at 802 cm^{-1}, has been assigned to this bond [22]. The C-H or C-O vibrations of the oxygen-hydrogen containing groups in the all magnetite nanoparticles were observed at 1348 cm^{-1} and 1475 cm^{-1}, respectively. It is notably observed that no distinct absorption bands typically associated with O-H stretching modes originating from hydroxyl groups or adsorbed moisture are present in the FTIR spectra in the 3000–3700 cm^{-1} range. The absence of these features indicates that the synthesized magnetite nanoparticles do not absorb moisture under storage conditions and have low hydroxyl content.

3.2. Morphological properties

Fig. 3 presents the morphological characterization of the core@shell

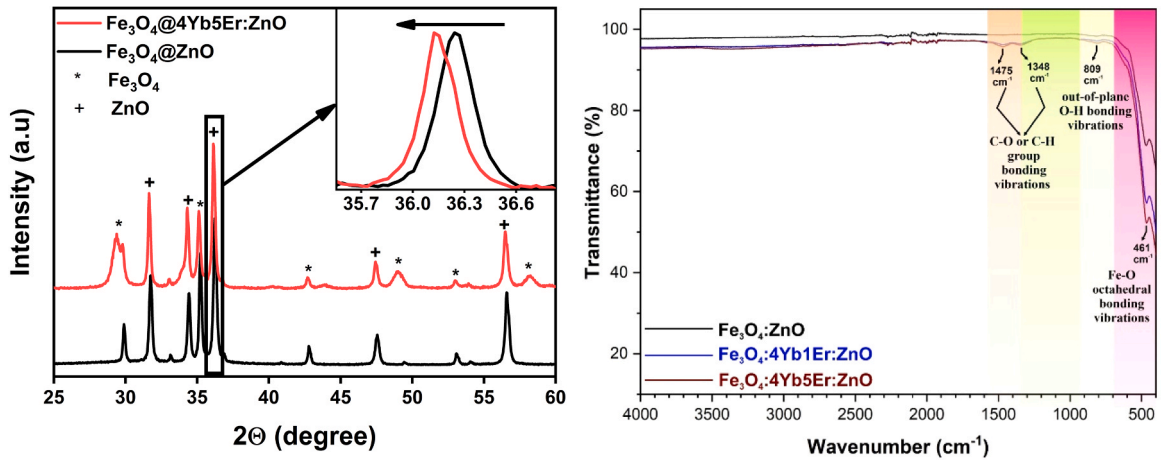

Fig. 2. (a) XRD patterns of core@shell Fe_3O_4@ZnO, and Fe_3O_4@4Yb5Er:ZnO composite nanoparticles and (b) FT-IR analysis of Fe_3O_4@ZnO, Fe_3O_4@4Yb1Er:ZnO, and Fe_3O_4@4Yb5Er:ZnO nanocomposites.

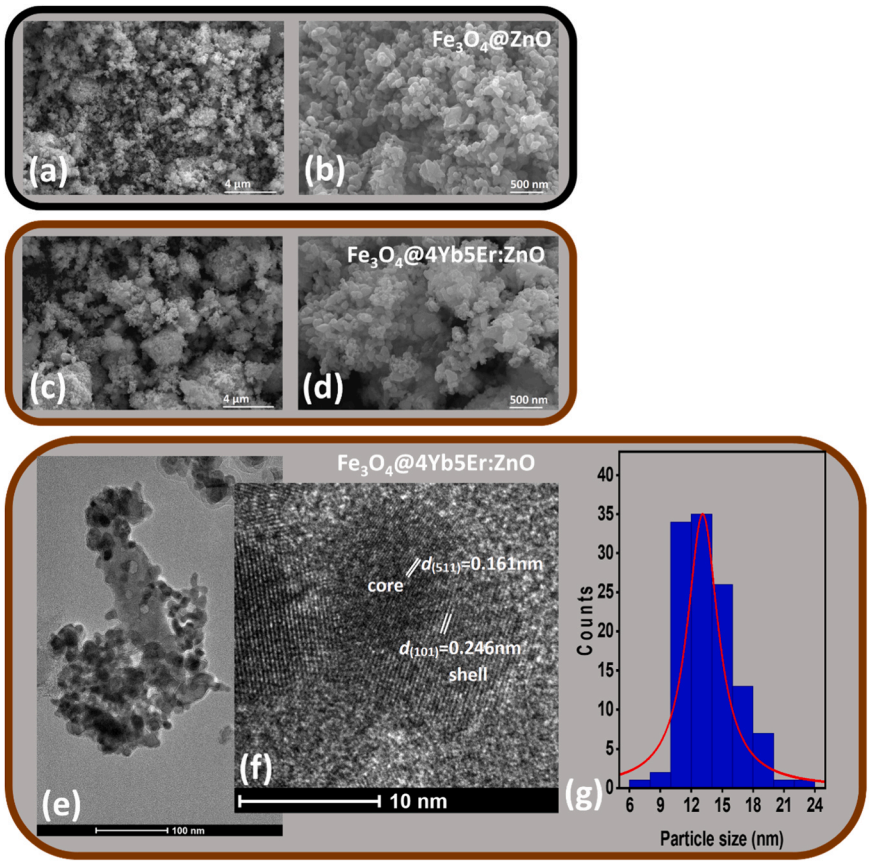

Fig. 3. SEM images of Fe_3O_4@ZnO nanocomposites at (a) 20,000x and (b) 100,000x magnification. SEM images of Fe_3O_4@4Yb5Er:ZnO nanocomposites at (c) 20,000x and (d) 100,000x magnification. (e) TEM image and (f) HR-TEM image and (g) particle size distribution histogram of Fe_3O_4@4Yb5Er:ZnO nanocomposites.

structured nanoparticles using SEM, TEM, and HR-TEM analyses. The SEM micrographs of Fe_3O_4@ZnO (Fig. 3a,b) and Fe_3O_4@4Yb5Er:ZnO (Fig. 3c,d) recorded at 20,000x and 100,000x magnifications reveal that the nanoparticles exhibit a nearly spherical morphology with a strong tendency to form agglomerates. Compared to Fe_3O_4@ZnO, the Yb/Er-doped sample displays denser clustering, which can be attributed to changes in surface energy induced by lanthanide incorporation. The TEM image of Fe_3O_4@4Yb5Er:ZnO (Fig. 3e) further confirms the agglomerative nature of the nanoparticles and highlights that the individual particle size remains in the nanometer range (~12 nm, as estimated by ImageJ analysis). The HR-TEM image (Fig. 3f) clearly validates the core/shell architecture, with distinct contrast between the Fe_3O_4 core and the Yb/Er-doped ZnO shell. The measured lattice fringes correspond to $d_{(511)}$= 0.161 nm for the cubic magnetite (Fe_3O_4) core and $d_{(101)}$= 0.246 nm for the hexagonal ZnO shell, confirming the crystalline nature of both regions. In addition, the particle size distribution histogram derived from TEM measurements is presented in Fig. 3g, demonstrating a narrow size distribution centered around ~12 nm. These findings are in good agreement with the XRD results, substantiating the successful synthesis of crystalline Fe_3O_4@ZnO-based core/shell nanocomposites with lanthanide doping. The average particle size of the core@shell nanocomposites was determined to be approximately 12 nm from TEM measurements, and this value is in good agreement with the particle dimensions observed in the HR-TEM images

3.3. Magnetic properties

The field-dependent magnetization curves of Fe_3O_4@ZnO, Fe_3O_4@4Yb1Er:ZnO, and Fe_3O_4@4Yb5Er:ZnO nanocomposites, recorded using a vibrating sample magnetometer (VSM, Lakeshore 7407) at room temperature, are shown in Fig. 4. All samples display nearly linear

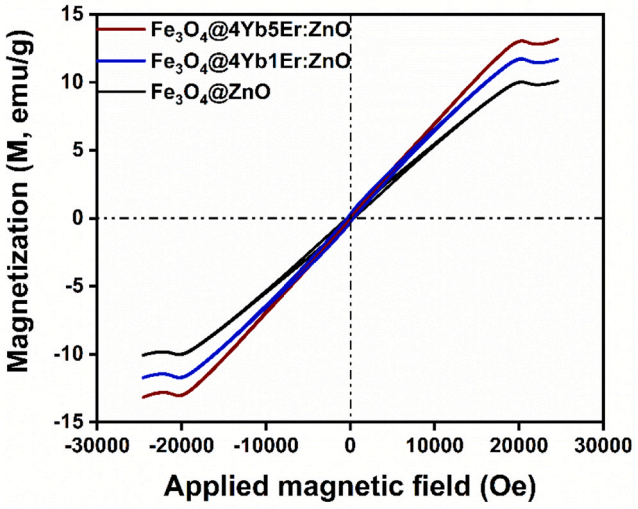

Fig. 4. Magnetization behavior of Fe_3O_4@ZnO, Fe_3O_4@4Yb1Er:ZnO, and Fe_3O_4@4Yb5Er:ZnO nanocomposites.

M-H behavior passing through the origin, with negligible coercivity (H_c) and remanent magnetization (M_r), indicating superparamagnetic-like soft magnetic characteristics. However, the absence of the typical sigmoidal saturation profile generally observed in strongly magnetic superparamagnets suggests that the response more closely resembles weak paramagnetism. This behavior can be ascribed to the presence of the nonmagnetic ZnO shell and the incorporation of Yb^{3+}/Er^{3+} dopants, both of which significantly reduce the effective magnetic contribution of

the Fe_3O_4 core. Nevertheless, the slight curvature observed at higher fields confirms that the Fe_3O_4 core still contributes to the overall magnetization, although its effect is suppressed. Among the samples, the magnetization follows the order Fe_3O_4@4Yb5Er:ZnO > Fe_3O_4@4Yb1Er:ZnO > Fe_3O_4@ZnO, indicating that the Fe_3O_4@4Yb5Er:ZnO sample exhibits the strongest magnetic response among the studied compositions. This enhancement is attributed to the additive paramagnetism of the rare-earth ions as well as possible dopant-induced interfacial effects, suggesting that controlled lanthanide incorporation provides an effective strategy to tune the magnetic behavior of such core@shell architectures for biomedical applications.

3.4. Optical properties

Fe_3O_4@ZnO host-based Yb^{3+}, Er^{3+} upconversion nano particles (UCNPs) system was formed, and Yb^{3+} ions were selected as sensitizers due to their broad absorption cross-section at 980 nm [23] [24]. Fig. 5a shows the UC luminescence spectrum of the prepared Fe_3O_4:Yb,Er:ZnO nanoparticles, and Fig. 4b shows the possible energy transfer phenomenon. Under 980 nm NIR laser diode irradiation, Yb^{3+} ions can absorb a photon energy and transition from the $^2F_{7/2}$ level to the $^2F_{5/2}$ level, where they can become populated. Yb^{3+} ions can transfer energy to surrounding Er^{3+} ions, causing Er^{3+} ions to transition from the $^4I_{15/2}$ level to the $^4I_{11/2}$ level. Some of the electrons at the $^4I_{11/2}$ level are arranged into the $^4I_{13/2}$ level of Er^{3+} ions via non-radiative transitions. Electrons at the $^4I_{13/2}$ energy level continue to absorb energy transferred by surrounding Yb^{3+} ions and transition from the $^4I_{13/2}$ level to the $^4F_{9/2}$ energy level. The $^4F_{9/2} \rightarrow {}^4I_{15/2}$ radiative transition emits red UCL peak at 659 nm. Some of the electrons at the $^4I_{11/2}$ energy level continue to absorb energy provided by Yb^{3+} ions and are arranged at the $^4F_{7/2}$ energy level. Electrons at the $^4F_{7/2}$ level are arranged at the $^2H_{11/2}$ and $^4S_{3/2}$ levels via non-radiative transitions. The $^2H_{11/2} \rightarrow {}^4I_{15/2}$ and $^4S_{3/2} \rightarrow {}^4I_{15/2}$ radiative transitions emit green UCL peaks at 523 nm and 542 nm. As shown in more detail in the figure, the intensity and transition positions of the observed luminescence transitions are quite consistent with published literature reports [25] [26]. During irradiation of Fe_3O_4@Yb,Er:ZnO upconversion nanoparticles with a NIR 980 nm laser diode, Yb^{3+} acted as an absorber (sensitizer), absorbing NIR photons and transferring the energy photons to the nearby activator Er^{3+} ion, thereby occupying the excited states of the emitter Er^{3+} ion ($^2H_{9/2}$, $^4S_{3/2}$, $^4F_{9/2}$). The cross-relaxation procedure of the $^4S_{3/2} \rightarrow {}^4I_{15/2}$ and $^4F_{9/2} \rightarrow {}^4I_{15/2}$ transitions is thought to play an important role in filling these emission transitions. Subsequently, the ground state can transition to the $^4I_{15/2}$ level via the $^2F_{5/2} \rightarrow {}^2F_{7/2}$ (Yb^{3+}):$^4S_{3/2} \rightarrow {}^4I_{15/2}$ and $^4F_{9/2} \rightarrow {}^4I_{15/2}$ Er^{3+} ion transitions. The phenomenon of energy transfer from ytterbium to erbium is quite consistent with the experimental observations obtained and is attributed to the effective population of Er^{3+} ions in the $^4S_{3/2}$ high-energy state. The strongest transition in the spectrum is centered at 542 nm ($^4S_{3/2} \rightarrow {}^4I_{15/2}$), and the upconversion nanoparticles exhibit bright green emission under 980 nm NIR laser diode irradiation [27]. As the concentration of Er^{3+} ions in the host material increases, the interactions between the dispersed Yb^{3+} and Er^{3+} ions within the structure, and consequently the energy transfer process from Yb^{3+} to Er^{3+}, follow a controlled increase phenomenon. The increase in UCL density reduces the distribution area of Er^{3+}/Yb^{3+} interaction and, accordingly, decreases the cross-relaxation probability, which increases the intensity of the bright green color of pure green UC luminescence [28]. The Fe_3O_4@Yb,Er:ZnO used in this article, with its spatial distribution and bright, intense green color, could be a promising candidate for UCL displays in photonic applications.

3.5. MTT-based assessment of Fe_3O_4@Yb:Er:ZnO nanocomposites on HUVEC viability

The effects of Fe_3O_4@4Yb1Er:ZnO, Fe_3O_4@4Yb3Er:ZnO, and Fe_3O_4@4Yb5Er:ZnO nanocomposites on HUVEC viability were evaluated using the MTT assay at 24, 48, and 72 h. All nanomaterials influenced cell viability in a concentration- and time-dependent manner (Fig. 6).

For Fe_3O_4@4Yb1Er:ZnO, at 24 h compared to the control group, a slight proliferative increase was observed at 50 and 100 μg/mL, whereas cell viability markedly decreased at 200 μg/mL and higher; although a slight increase was seen at 800 μg/mL, viability remained well below that of the control. At 48 h, cell viability decreased at 50 μg/mL compared to the control, while cytotoxicity persisted at medium and high doses, with slight recovery observed at 400–800 μg/mL. At 72 h, the proliferative effect at low doses disappeared relative to the control, cell viability remained reduced at medium doses, and slight increases or partial recovery were observed at 400 and 800 μg/mL.

For Fe_3O_4@4Yb3Er:ZnO, at 24 h compared to the control group, a slight increase in cell viability was observed at 50 μg/mL, while at 100 μg/mL viability was close to the control but slightly reduced.

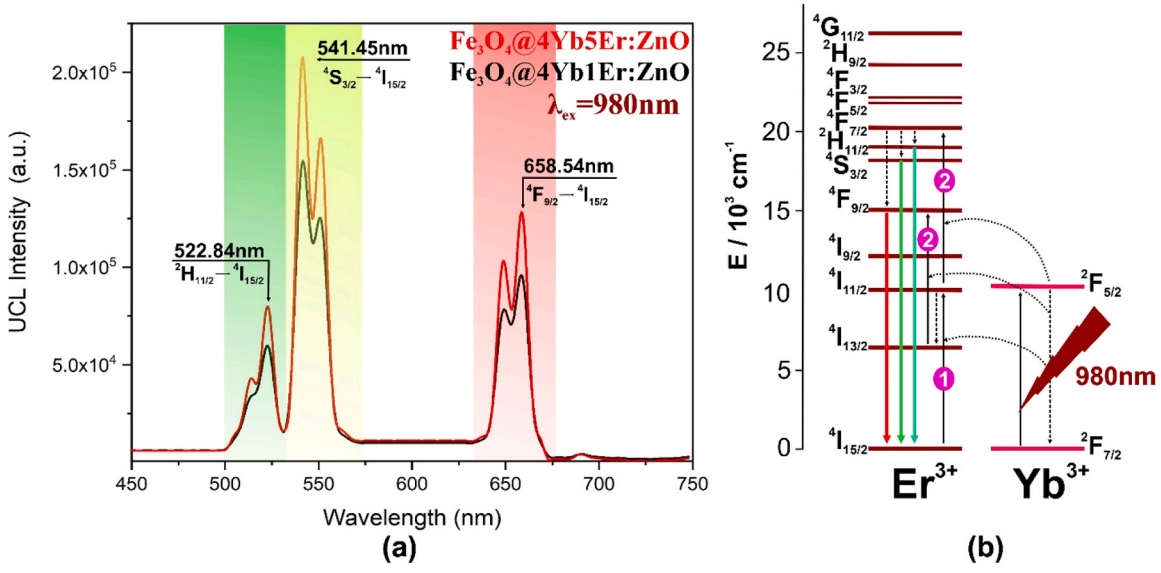

Fig. 5. (a) UC spectra of Fe_3O_4@4Yb1Er:ZnO and Fe_3O_4@4Yb5Er:ZnO core@shell under the excitation of 980 nm continuous pump light and (b) Schematic diagram of energy transfer process in Fe_3O_4:4Yb1Er:ZnO UCNPs.

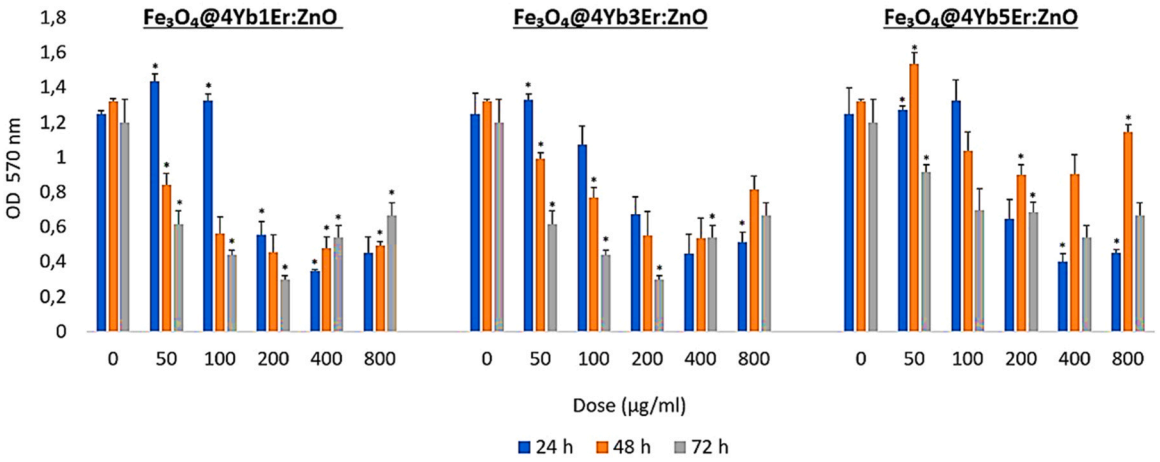

Fig. 6. Evaluation of HUVEC cell viability after 24, 48, and 72 h of incubation with Fe_3O_4@4Yb1Er:ZnO, Fe_3O_4@4Yb3Er:ZnO, and Fe_3O_4@4Yb5Er:ZnO nanocomposites using the MTT assay. Data are presented as mean ± standard deviation (n = 3). Statistical significance was considered at $p < 0.05$.

Marked cytotoxicity was observed at 200, 400 µg/mL, and higher doses; although a slight increase was seen at 800 µg/mL, viability remained below that of the control. At 48 h, cell viability decreased at the low dose compared to the control, while cytotoxicity persisted at medium and high doses; partial recovery was observed at 800 µg/mL, but viability remained lower than the control. At 72 h, cytotoxic effects continued at 50, 100, and 200 µg/mL, whereas slight increases in viability were observed at 400 and 800 µg/mL, although values remained below the control.

For Fe_3O_4@4Yb5Er:ZnO, at 24 h compared to the control group, cell viability was above baseline at 50 and 100 µg/mL, indicating a strong short-term proliferative effect, whereas a decrease in viability was observed at 200–800 µg/mL. At 48 h, the proliferative effect at 50 µg/mL persisted relative to the control, while decreases were observed at 100, 200, and 400 µg/mL; partial recovery was noted at 800 µg/mL. At 72 h, marked decreases in cell viability were observed at 50–400 µg/mL, whereas a slight increase or recovery was observed at 800 µg/mL. The increases in cell viability at higher doses may be associated with adaptive cellular responses.

Overall, low concentrations elicited limited proliferative effects, while cytotoxicity predominated at 200 µg/mL and above. The 50 µg/mL dose was considered appropriate due to its proliferative effect, potentially resulting from low-concentration metabolic stimulation or adaptive cellular responses supporting proliferation. As marked proliferation decline was observed at 72 h, subsequent gene expression analyses were performed at 24 and 48 h to ensure reliable comparisons.

3.6. *Effect of Fe_3O_4@Yb:Er:ZnO nanocomposites on HUVEC cell migration*

The effects of Fe_3O_4@4Yb1Er:ZnO, Fe_3O_4@4Yb3Er:ZnO, and Fe_3O_4@4Yb5Er:ZnO nanomaterials on HUVEC cell migration were investigated using the scratch assay. All data are presented as the mean of three independent experiments and expressed as percentages (%). In the control group, cell migration was set at 100 %, whereas it was 84.25 % for Fe_3O_4@4Yb1Er:ZnO and 89.17 % for Fe_3O_4@4Yb3Er:ZnO. In the Fe_3O_4@4Yb5Er:ZnO-treated group, migration was equivalent to the control level (100 %); this equivalence indicates that the treatment does not exert any inhibitory effect on cell proliferation and that HUVEC cells maintain their normal migratory capacity (Fig. 7).

3.7. *The proliferation and angiogenic response of HUVEC cells to Fe_3O_4@YbEr:ZnO treatment*

The expression profiles of proliferation- and angiogenesis-related genes in HUVEC cells in response to Fe_3O_4@4YbEr:ZnO treatments were evaluated over time. VEGF expression is shown in Fig. 8a. Fe_3O_4@4Yb1Er:ZnO treatment resulted in a 1.14-fold increase at 24 h ($p = 0.029$), which declined to 0.95-fold at 48 h approaching control levels ($p = 0.037$). In the Fe_3O_4@4Yb3Er:ZnO group, VEGF expression

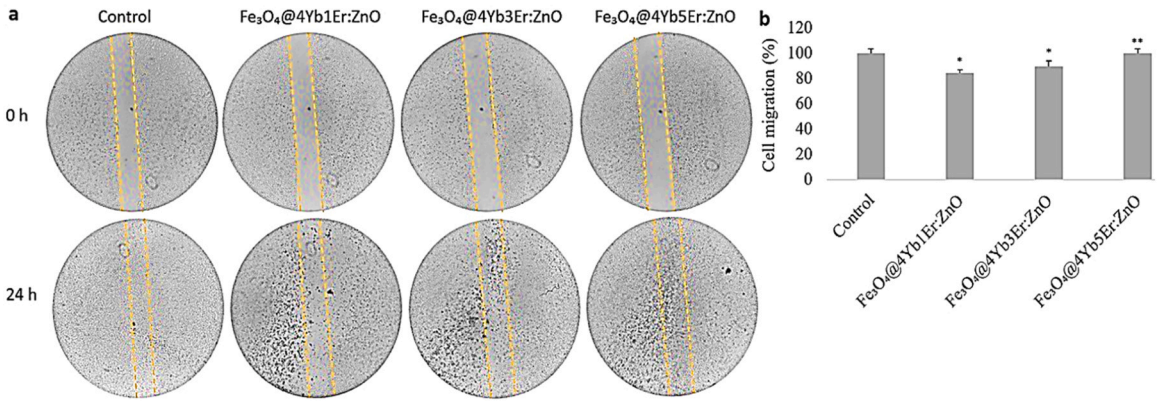

Fig. 7. Effect of Fe_3O_4@4Yb1Er:ZnO, Fe_3O_4@4Yb3Er:ZnO, and Fe_3O_4@4Yb5Er:ZnO nanocomposites on HUVEC Cell Migration. (a) Representative images of the scratch assay. The upper panels show the cell monolayer immediately after scratch creation (0 h), while the lower panels depict cell migration 24 h post-scratch. Grey dashed lines were added to visually track the closure dynamics of the wound area. (b) Quantitative analysis of cell migration. Migration rates were calculated as percentages relative to the control group, and statistical significance was considered at $^*p < 0.05$, $^{**}p < 0.01$, and $^{***}p < 0.001$.

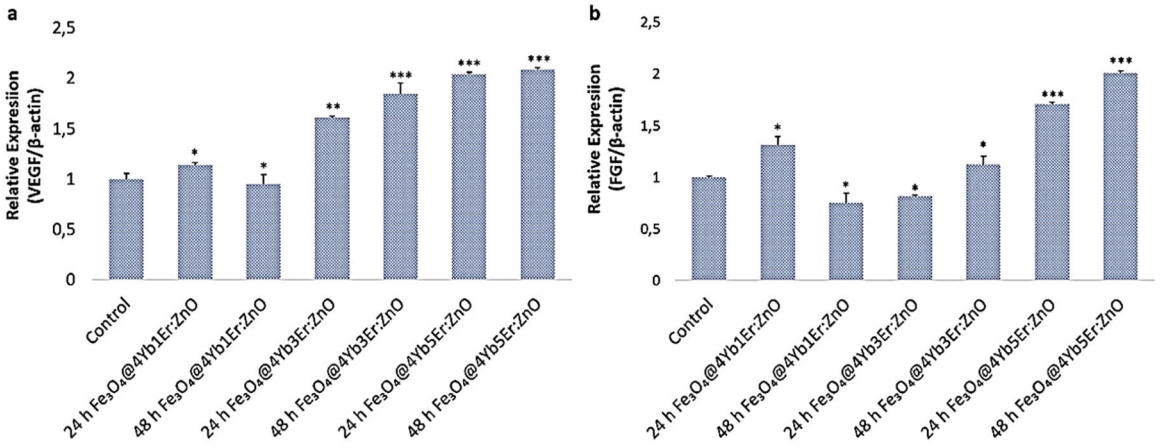

Fig. 8. VEGF and FGF mRNA expression in HUVEC cells after Fe_3O_4@4YbEr:ZnO treatment.(a) VEGF mRNA expression levels at 24 and 48 h following treatment with Fe_3O_4@4Yb1Er:ZnO, Fe_3O_4@4Yb3Er:ZnO, and Fe_3O_4@4Yb5Er:ZnO (b) FGF mRNA expression levels at 24 and 48 h for the same treatment groups. Data are presented as fold change relative to control. All values represent mean ± SD of three independent experiments. Statistical significance is indicated: *$p < 0.05$, **$p < 0.01$, ***$p < 0.001$ versus control.

increased 1.61-fold at 24 h ($p = 0.008$) and 1.85-fold at 48 h ($p < 0.001$). The most pronounced effect was observed with Fe_3O_4@4Yb5Er:ZnO, showing a 2.04-fold increase at 24 h and a 2.08-fold increase at 48 h ($p < 0.001$). FGF expression is presented in Fig. 8b. Fe_3O_4@4Yb1Er:ZnO induced a 1.32-fold increase at 24 h ($p = 0.041$), which decreased to 0.75-fold at 48 h ($p = 0.044$). In the Fe_3O_4@4Yb3Er:ZnO group, a 0.81-fold decrease was observed at 24 h ($p = 0.011$), followed by a 1.12-fold increase at 48 h ($p = 0.034$). The highest induction was seen in the Fe_3O_4@4Yb5Er:ZnO group, with a 1.71-fold increase at 24 h and a 2.01-fold increase at 48 h ($p < 0.001$).

MMP-3 expression is illustrated in Fig. 9a. All treatment groups showed significant increases. Fe_3O_4@4Yb1Er:ZnO resulted in a 2.17-fold increase at 24 h ($p = 0.004$) and a 3.25-fold increase at 48 h ($p = 0.009$). In the Fe_3O_4@4Yb3Er:ZnO group, expression increased 3.22-fold at 24 h ($p = 0.006$) and 3.68-fold at 48 h ($p = 0.007$). The strongest effect was observed with Fe_3O_4@4Yb5Er:ZnO, showing a 5.85-fold increase at 24 h and a 5.31-fold increase at 48 h ($p < 0.001$). MMP-9 expression is presented in Fig. 9b and exhibited a similar trend. In the Fe_3O_4@4Yb1Er:ZnO group, expression increased 1.63-fold at 24 h ($p = 0.008$) and 3.05-fold at 48 h ($p < 0.001$). Fe_3O_4@4Yb3Er:ZnO treatment resulted in a 2.74-fold increase at 24 h ($p = 0.004$), followed by a decrease to 1.94-fold at 48 h ($p = 0.017$). The highest levels were observed in the Fe_3O_4@4Yb5Er:ZnO group, with a 5.53-fold increase at 24 h ($p < 0.001$) and a 3.63-fold increase at 48 h ($p = 0.002$).

3.8. Antibacterial activity

The antibacterial activity results summarized in Table 3 demonstrate a clear difference in the response of Gram-negative *Escherichia coli* and Gram-positive *Staphylococcus aureus* to the synthesized nanocomposites. For *E. coli*, the inhibition zones remained relatively small (8.32–9.01 mm), indicating good antibacterial performance. This limited activity can be attributed to the protective effect of the lipopolysaccharide outer membrane of Gram-negative bacteria, which restricts nanoparticle penetration and reactive oxygen species (ROS) interaction. In contrast, *S. aureus* exhibited a much higher susceptibility, with inhibition zones ranging from 9.52 mm for undoped Fe_3O_4@ZnO to 13.53 mm for Fe_3O_4@4Yb3Er:ZnO. The substantial enhancement observed upon Yb/Er doping highlights the role of lanthanide incorporation in improving antibacterial efficacy, likely through increased ROS generation, enhanced charge separation, and surface state modifications. Interestingly, the highest dopant concentration (Fe_3O_4@4Yb5Er:ZnO) did not further improve antibacterial performance against *S. aureus*, suggesting a dopant saturation effect, where excessive doping may introduce defect clustering and reduce the number of active reactive sites. Overall, these findings confirm that Yb/Er co-doping

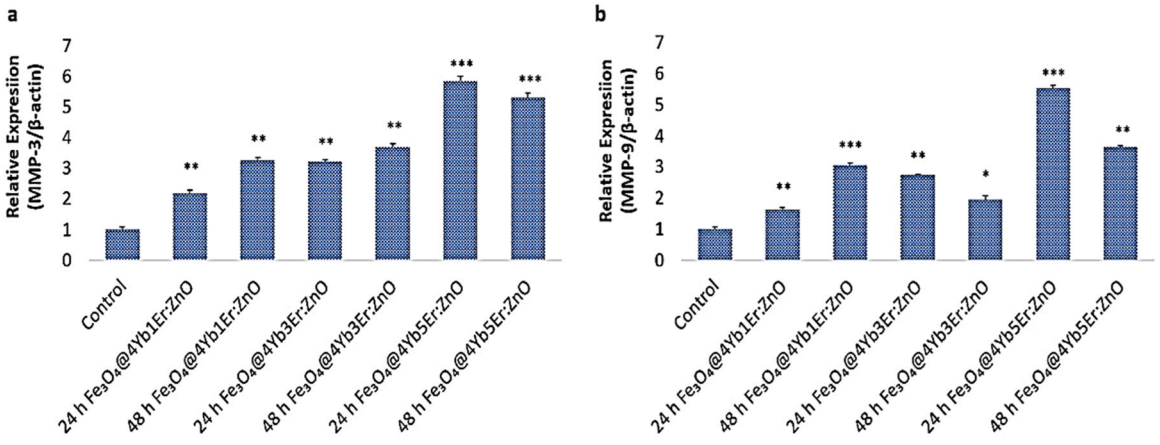

Fig. 9. MMP-3 and MMP-9 mRNA expression in HUVEC cells after Fe_3O_4@4YbEr:ZnO treatment.(a) MMP-3 mRNA expression levels at 24 and 48 h following treatment with Fe_3O_4@4Yb1Er:ZnO, Fe_3O_4@4Yb3Er:ZnO, and Fe_3O_4@4Yb5Er:ZnO (b) MMP-9 mRNA expression levels at 24 and 48 h for the same treatment groups. Data are presented as fold change relative to control. Values represent mean ± SD of three independent experiments. Statistical significance is indicated: *$p < 0.05$, **$p < 0.01$, ***$p < 0.001$ versus control.

Table 3
Antibacterial activities of composite nanoparticles and its derivatives against *E. coli* and *S. aureus* bacteria by well-diffusion method. Antibacterial activity results were measured as inhibition zones, and mm was used as the unit for the diameter of the wells.

	Fe_3O_4@ZnO	Fe_3O_4@4Yb1Er:ZnO	Fe_3O_4@4Yb3Er:ZnO	Fe_3O_4@4Yb5Er:ZnO
E. coli	8.64 ± 0.69	8.32 ± 0.29	8.56 ± 0.46	9.01 ± 0.70
S. aureus	9.52 ± 1.13	13.03 ± 0.75	13.53 ± 1.07	11.99 ± 1.17

significantly strengthens antibacterial activity, particularly against Gram-positive strains, and that an optimal dopant concentration is crucial for maximizing biological performance.

The successful synthesis of Fe_3O_4@ZnO and Yb/Er-doped Fe_3O_4@ZnO core@shell nanocomposites has been confirmed through a combination of structural, morphological, magnetic, optical and antibacterial analyses. The XRD results demonstrated the coexistence of the cubic Fe_3O_4 core and the hexagonal ZnO shell without secondary phases, confirming high crystallinity and phase purity. The shift of the ZnO (101) peak towards lower diffraction angles upon Yb^{3+}/Er^{3+} doping indicated lattice expansion due to the substitution of Zn^{2+} by larger lanthanide ions, further validating successful incorporation of dopants into the shell structure. FTIR spectra corroborated these findings by identifying characteristic Fe-O and Zn-O vibrations while showing the absence of hydroxyl-related absorptions, suggesting good stability and low surface hydroxylation.

Morphological analysis using SEM and TEM revealed nearly spherical particles with a strong agglomeration tendency, particularly in doped samples. This enhanced clustering is likely associated with surface energy modifications induced by lanthanide incorporation. TEM and HR-TEM imaging provided direct evidence of the core@shell structure, with distinct lattice fringes corresponding to Fe_3O_4 and ZnO, supporting the XRD observations.

Magnetic studies further emphasized the influence of the ZnO shell and lanthanide doping on the magnetic response. All samples exhibited negligible coercivity and remanence, consistent with superparamagnetic-like soft magnetic behavior. However, the absence of a sigmoidal saturation profile revealed a weakly paramagnetic trend, attributed to suppression of the Fe_3O_4 core contribution by the ZnO shell and dopants. The order of magnetization, Fe_3O_4@4Yb5Er:ZnO > Fe_3O_4@4Yb1Er:ZnO > Fe_3O_4@ZnO, suggests that Yb^{3+}/Er^{3+} ions not only contribute additive paramagnetism but also enhance interfacial spin interactions. These findings confirm that doping not only modifies magnetic strength but also tunes spin interactions at the core@shell boundary.

The optical analysis highlighted efficient energy transfer from Yb^{3+} to Er^{3+} ions, producing strong green emission at 542 nm under 980 nm excitation along with red luminescence at 659 nm. The enhancement of upconversion luminescence intensity with higher Er^{3+} content confirmed effective sensitizer-activator coupling within the ZnO host. These findings align well with previous studies on lanthanide-doped ZnO nanostructures and emphasize their suitability for bioimaging and photonic applications. Moreover, when combined with the tunable magnetic properties, the optical performance highlights the potential of these nanocomposites as multifunctional platforms for integrated imaging and therapeutic applications.

Antibacterial assays highlighted selective inhibition of Gram-positive *S. aureus* relative to Gram-negative *E. coli*, attributable to differences in bacterial cell wall structures. While the lipopolysaccharide barrier in Gram-negative bacteria restricts nanoparticle penetration, Gram-positive bacteria are more vulnerable to ROS-mediated damage. Doping with Yb^{3+}/Er^{3+} enhanced antibacterial efficacy, particularly at intermediate levels, due to improved ROS generation and charge separation. At higher doping levels, however, activity declined, likely due to dopant clustering and saturation effects. Interestingly, while the highest magnetization was observed for Fe_3O_4@4Yb5Er:ZnO, the strongest antibacterial activity was obtained at the intermediate Fe_3O_4@4Yb3Er:ZnO composition, indicating that optimal doping levels depend on the targeted functionality.

The *in vitro* cytocompatibility studies provided further insights into biological performance. MTT analyses demonstrated that the nanomaterials affected HUVEC cell viability in both a dose- and time-dependent manner. Low-dose treatments (50 μg/mL) promoted cell proliferation, whereas higher doses (≥200 μg/mL) induced significant cytotoxicity. These findings suggest that the nanocomposites can stimulate cellular metabolism and enhance proliferation at lower concentrations while adversely affecting cell health at higher concentrations. Cell migration assays revealed that the Fe_3O_4@4Yb5Er:ZnO-treated group exhibited migration levels comparable to the control group, indicating that this treatment does not inhibit HUVEC migration. In contrast, migration rates in the Fe_3O_4@4Yb1Er:ZnO and Fe_3O_4@4Yb3Er:ZnO groups were slightly lower, suggesting that nanomaterials with lower Yb/Er content may partially restrict HUVEC migratory capacity, whereas higher doping levels (Fe_3O_4@4Yb5Er:ZnO) preserve normal migration. Consistent with these results, previous studies have shown that iron oxide nanoparticles can enhance the migratory capacity of mesenchymal stem cells and support their homing to injury or wound sites [29].

Gene expression analyses demonstrated significant upregulation of angiogenesis-related growth factors, including VEGF and FGF, particularly in the Fe_3O_4@4Yb5Er:ZnO group. This upregulation is consistent with the proliferation and migration results and suggests that the nanomaterials may promote vascular growth and remodeling in endothelial cells. Similarly, ZnO and CuO nanoparticles have been reported to enhance VEGF expression in HUVEC cells, and luminescent ruthenium-modified selenium nanoparticles (Ru-SeNPs) have been shown to induce angiogenesis and FGF expression [30–32]. MMP-3 and MMP-9 expression was also markedly increased, especially in the Fe_3O_4@4Yb5Er:ZnO group, indicating that these nanocomposites may facilitate extracellular matrix remodeling and genetically support endothelial migratory capacity. While non-cytotoxic doses (0.5 and 1 μg/mL) of Nano-CuO have been reported to increase MMP-3 expression and activity in conditioned media of BEAS-2B and U937 cells, studies on MMP expression induced by ZnO nanoparticles remain limited, highlighting the originality and innovative contribution of our work [33]. These results highlight the ability of lanthanide-doped Fe_3O_4@ZnO nanocomposites to modulate endothelial cell proliferation, migration and angiogenesis, key processes in tissue regeneration and vascular remodeling. These biological findings not only demonstrate efficacy of the developed nanocomposites but also align with the objectives of the United Nations Sustainable Development Goal 3 (Good Health and Well-Being), which aims to promote health, prevent infections, and advance innovative biomedical technologies [34].

Collectively, these findings demonstrate that controlled lanthanide incorporation into Fe_3O_4@ZnO nanocomposites tailors multifunctional performance across structural, magnetic, optical, antibacterial, and cellular domains. The capacity to balance magnetic tunability, upconversion luminescence, antibacterial efficacy, and pro-angiogenic cellular responses underscores the promise of these nanocomposites as advanced multifunctional platforms for biomedical theranostics, regenerative medicine, and antimicrobial applications.

4. Conclusions

This study demonstrates the successful synthesis and comprehensive evaluation of Fe_3O_4@ZnO and Yb/Er-doped Fe_3O_4@ZnO core@shell

nanocomposites as multifunctional nanoplatforms for biomedical applications. Structural analyses confirmed the formation of phase-pure cubic Fe_3O_4 cores and hexagonal ZnO shells, while systematic shifts in the ZnO lattice parameters verified the effective incorporation of Yb^{3+} and Er^{3+} ions. Morphological investigations revealed nanoscale core@shell architectures with increased agglomeration upon lanthanide doping consistent with dopant-induced surface energy modifications.

Magnetic measurements showed superparamagnetic-like behavior with negligible coercivity and remanence for all samples, while lanthanide incorporation enabled tunable magnetic responses. Among the studied compositions, Fe_3O_4@4Yb5Er:ZnO exhibited the highest magnetization, highlighting the additive paramagnetic contribution of rare-earth ions and their influence on interfacial spin interactions. Optical characterization demonstrated efficient Yb^{3+}→Er^{3+} energy transfer under 980 nm excitation, producing intense green and red upconversion luminescence, thereby confirming the suitability of these nanocomposites for near-infrared-triggered bioimaging applications.

Biological evaluations revealed a clear functionality-dependent response to lanthanide concentration. Antibacterial assays showed selective inhibition of Gram-positive *S. aureus*, with maximum activity observed at the intermediate Fe_3O_4@4Yb3Er:ZnO composition, while *E. coli* exhibited lower susceptibility. *In vitro* cytocompatibility, migration and gene expression analyses demonstrated that Fe_3O_4@4Yb5Er:ZnO promotes endothelial cell migration, upregulates angiogenic factors (VEGF and FGF), and enhances extracellular matrix remodeling through increased MMP-3 and MMP-9 expression, indicating its potential to support tissue regeneration and vascular remodeling.

Overall, these results provide clear evidence that optimal lanthanide doping is strongly property-dependent and enables precise tailoring of magnetic, optical, antibacterial, and biological functionalities within a single nanosystem. The integration of tunable magnetism, NIR-excited upconversion luminescence, selective antibacterial activity, and pro-angiogenic cellular responses underscores the promise of Yb/Er-doped Fe_3O_4@ZnO nanocomposites as advanced multifunctional platforms for theranostic and regenerative medicine applications, contributing to the objectives of the United Nations Sustainable Development Goal 3 (Good Health and Well-Being).

CRediT authorship contribution statement

Sinem Gultekin Tosun: Writing – original draft, Methodology. **Mehmet Emin Diken:** Methodology. **Umit Huseyin Kaynar:** Data curation. **Selin Bayram:** Methodology. **Akyel Mehmet Fatih:** Methodology. **Mustafa Burak Coban:** Writing – original draft, Methodology. **Ayla Solmaz Avcikurt:** Writing – original draft, Methodology. **Ünal Fatma:** Writing – original draft, Visualization, Validation, Supervision, Resources, Project administration, Methodology, Investigation, Funding acquisition, Formal analysis, Data curation, Conceptualization.

Declaration of Competing Interest

The authors declare that they have no known competing financial interests or personal relationships that could have appeared to influence the work reported in this paper.

Acknowledgments

This study was supported by The Scientific and Technological Research Council of Turkey (TÜBİTAK) under the 2209-A Research Project Support Programme for Undergraduate Students (Project No: 1919B012320255), and the authors would like to express their sincere gratitude for this funding.

References

[1] S. Laurent, et al., Magnetic iron oxide nanoparticles: synthesis, stabilization, vectorization, physicochemical characterizations, and biological applications, Chem. Rev. 108 (6) (Jun. 2008) 2064–2110, https://doi.org/10.1021/cr068445e.
[2] F. Unal, B. Ercan, Magnetic and luminescence properties of bioactive glass nanoparticles for biomedical applications, J. Aust. Ceram. Soc. 61 (Mar. 2025) 301–310, https://doi.org/10.1007/s41779-024-01141-4.
[3] J.F. Jeevakumari, G. Suresh, Comprehensive evaluation of solvothermally synthesized Fe3O4 and PEG capped Fe3O4 nanoparticles for magnetic and biomedical applications, Inorg. Chem. Commun. 174 (2025) 113904, https://doi.org/10.1016/j.inoche.2025.113904.
[4] S. Ahmadi, C.H. Chia, S. Zakaria, K. Saeedfar, N. Asim, Synthesis of Fe 3O 4 nanocrystals using hydrothermal approach, J. Magn. Magn. Mater. 324 (2012) 4147–4150, https://doi.org/10.1016/j.jmmm.2012.07.023.
[5] Y.-X.J. Wang, Superparamagnetic iron oxide based MRI contrast agents: current status of clinical application, Quant. Imaging Med. Surg. 1 (1) (2011) 35–40, https://doi.org/10.3978/j.issn.2223-4292.2011.08.03.
[6] J. Estelrich, E. Escribano, J. Queralt, M.A. Busquets, Iron oxide nanoparticles for magnetically-guided and magnetically-responsive drug delivery, Int. J. Mol. Sci. 16 (2015) 8070–8101, https://doi.org/10.3390/ijms16048070.
[7] P.R. Oskoui, M. Rezvani, Revolution in cancer treatment methods: perspective review of factors affecting the final results of nanoparticles used in magnetic fluid hyperthermia, Heal. Sci. Rev. 14 (2025) 100212, https://doi.org/10.1016/j.hsr.2025.100212.
[8] M. Mahmoudi, H. Hofmann, B. Rothen-Rutishauser, A. Petri-Fink, Assessing the in vitro and in vivo toxicity of superparamagnetic iron oxide nanoparticles, Chem. Rev. 112 (2012) 2323–2338, https://doi.org/10.1021/cr2002596.
[9] S. Girish Kumar, R. Kavitha, Lanthanide ions doped ZnO based photocatalysts, Sep. Purif. Technol. 274 (2021) 118853, https://doi.org/10.1016/j.seppur.2021.118853.
[10] P. Pascariu, et al., Novel rare earth (RE-La, Er, Sm) metal doped ZnO photocatalysts for degradation of Congo-Red dye: synthesis, characterization and kinetic studies, J. Environ. Manag. 239 (2019) 225–234, https://doi.org/10.1016/j.jenvman.2019.03.060.
[11] A.S. Allogmani, R.M. Mohamed, M.S. Hasanin, Green, eco-friendly, highly biocompatible and bioactive nanocomposite-based biopolymers loaded with ZnO@Fe3O4 nanoparticles, Polymers 15 (2023) 3641, https://doi.org/10.3390/polym15173641.
[12] J. Gupta, P.A. Hassan, K.C. Barick, Core-shell Fe3O4@ZnO nanoparticles for magnetic hyperthermia and bio-imaging applications, AIP Adv. 11 (2021) 025207, https://doi.org/10.1063/9.0000135.
[13] A. Sirelkhatim, et al., Review on zinc oxide nanoparticles: antibacterial activity and toxicity mechanism, NanoMicro Lett. 7 (3) (2015) 219–242, https://doi.org/10.1007/s40820-015-0040-x.
[14] A. Manikandan, et al., Structural, morphological and optical properties of multifunctional magnetic-luminescent ZnO@Fe3O4 nanocomposite, Phys. E Low. Dimens. Syst. Nanostruct. 124 (2020) 114291, https://doi.org/10.1016/j.physe.2020.114291.
[15] F. Unal, Production and characterization of magnetic-luminescent Fe3O4@ZnO:RE composite nanoparticles for biomedical application, Phys. Status Solidi Appl. Res. 220 (2023) 1–6, https://doi.org/10.1002/pssa.202300149.
[16] Y. Li, R. Wang, W. Zheng, Y. Li, Silica-coated Ga(III)-Doped ZnO: Yb3+, Tm3+ upconversion nanoparticles for high-resolution in vivo bioimaging using near-infrared to near-infrared upconversion emission, Inorg. Chem. 58 (2019) 8230–8236, https://doi.org/10.1021/acs.inorgchem.9b01056.
[17] F. Wang, X. Liu, Recent advances in the chemistry of lanthanide-doped upconversion nanocrystals, Chem. Soc. Rev. 38 (2009) 976–989, https://doi.org/10.1039/b809132n.
[18] S. Hamdi, H. Smaoui, S. Guermazi, G. Leroy, B. Duponchel, Enhancing the structural, optical and electrical conductivity properties of ZnO nanopowders through Dy doping, Inorg. Chem. Commun. 144 (2022) 109819, https://doi.org/10.1016/j.inoche.2022.109819.
[19] F. Unal, K. Kazmanli, Production and characterization of RE3+:Yb2O3 nanoparticles, Mater. Sci. Forum 1034 (2021) 117–122, https://doi.org/10.4028/www.scientific.net/msf.1034.117.
[20] F. Unal, F. Kaya, K. Kazmanli, Synthesis, characterization and radioluminescence properties of erbium-doped yttria phosphors, Int. J. Miner. Metall. Mater. 28 (2021) 1983–1990, https://doi.org/10.1007/s12613-021-2269-3.
[21] Astuti, S. Arief, M. Muldarisnur, Zulhadjri, and S.R.A. Usna, "Enhancement in photoluminescence performance of carbon-based Fe3O4@ZnO–C nanocomposites," Vacuum, vol. 211, p. 111935, 2023, doi: 10.1016/j.vacuum.2023.111935.
[22] L. Zhang, R. He, H.C. Gu, Oleic acid coating on the monodisperse magnetite nanoparticles, Appl. Surf. Sci. 253 (5) (2006) 2611–2617, https://doi.org/10.1016/j.apsusc.2006.05.023.
[23] H. Cui, et al., Extremely intense green up-conversion luminescent and ultra-high temperature sensitivity in Er3+/Yb3+ co-doped BiTa7O19 phosphors, J. Lumin 241 (2022) 118484, https://doi.org/10.1016/j.jlumin.2021.118484.
[24] L. Li, et al., Excellent upconversion luminescence intensity in Er3+/Yb3+/Mo4+ triple-doped BiTa7O19 phosphors, J. Alloy. Compd. 938 (2023) 168725, https://doi.org/10.1016/j.jallcom.2023.168725.
[25] W. Niu, S. Wu, S. Zhang, J. Li, L. Li, Multicolor output and shape controlled synthesis of lanthanide-ion doped fluorides upconversion nanoparticles, Dalt. Trans. 40 (13) (2011) 3305–3314, https://doi.org/10.1039/c0dt01344g.

[26] Y. Wang, R. Cai, Z. Liu, Controlled synthesis of NaYF4: Yb, Er nanocrystals with upconversion fluorescence via a facile hydrothermal procedure in aqueous solution, CrystEngComm 13 (2011) 1772–1774, https://doi.org/10.1039/c0ce00708k.
[27] A.A. Ansari, J.P. Labis, A. Khan, Biocompatible NaYF4:Yb,Er upconversion nanoparticles: colloidal stability and optical properties, J. Saudi Chem. Soc. 25 (2021) 101390, https://doi.org/10.1016/j.jscs.2021.101390.
[28] X. Liu, et al., Pure green and pure red upconversion luminescence due to different distributions of Er3+/Yb3+ in tantalate, Radiat. Phys. Chem. 239 (2026) 113296, https://doi.org/10.1016/j.radphyschem.2025.113296.
[29] X. Li, Z. Wei, H. Lv, L. Wu, Y. Cui, H. Yao, J. Li, H. Zhang, B. Yang, J. Jiang, Iron oxide nanoparticles promote the migration of mesenchymal stem cells to injury sites, Int. J. Nanomed. 14 (2019) 573–589, https://doi.org/10.2147/IJN.S184920.
[30] N. Poier, et al., Effects of zinc oxide nanoparticles in huvec: Cyto-and genotoxicity and functional impairment after long-term and repetitive exposure in vitro, Int. J. Nanomed. 15 (2020) 4441–4452, https://doi.org/10.2147/IJN.S246797.
[31] P. Balasubramanian, A.J. Salinas, S. Sanchez-Salcedo, R. Detsch, M. Vallet-Regi, A. R. Boccaccini, Induction of VEGF secretion from bone marrow stromal cell line (ST-2) by the dissolution products of mesoporous silica glass particles containing CuO and SrO, J. Non Cryst. Solids 500 (2018) 217–224, https://doi.org/10.1016/j.jnoncrysol.2018.07.073.
[32] D. Sun, et al., The effects of luminescent ruthenium(II) polypyridyl functionalized selenium nanoparticles on bFGF-induced angiogenesis and AKT/ERK signaling, Biomaterials 34 (2013) 171–180, https://doi.org/10.1016/j.biomaterials.2012.09.031.
[33] Y. Zhang, Y. Mo, Y. Zhang, J. Yuan, Q. Zhang, MMP-3-mediated cleavage of OPN is involved in copper oxide nanoparticle-induced activation of fibroblasts, Part. Fibre Toxicol. 20 (2023) 1–21, https://doi.org/10.1186/s12989-023-00532-y.
[34] United Nations, Sustainable Development Goal 3: Good Health and Well-Being. United Nations Department of Economic and Social Affairs, ⟨https://sdgs.un.org/goals/goal3⟩ (accessed October 2025).